Publication Year	2024
Acceptance in OA	2025-01-21T15:25:35Z
Title	Deriving Mutual Impedance Matrix of a Large Antenna Array from Embedded Element Patterns with Measurement Noise
Authors	KYRIAKOU, Georgios, Kovaleva, Maria, Warnick, Karl F., Davidson, David B., BOLLI, Pietro
Publisher's version (DOI)	10.1109/TAP.2024.3470311
Handle	http://hdl.handle.net/20.500.12386/35688
Journal	IEEE TRANSACTIONS ON ANTENNAS AND PROPAGATION

Deriving Mutual Impedance Matrix of a Large Antenna Array from Embedded Element Patterns with Measurement Noise

Georgios Kyriakou, Maria Kovaleva, *Member, IEEE,* Karl F. Warnick, *Fellow, IEEE,*
David B. Davidson, *Fellow, IEEE,* and Pietro Bolli

***Abstract*—Measuring the *in situ* mutual impedance matrix of a large phased array with a quasi-random element layout is a very challenging operation. A recently developed method for extracting the impedance matrix of a phased array of antennas from its embedded element patterns is implemented and tested with a cluster of 16 log-periodic antennas that served as a Square Kilometer Array (SKA) prototype. The extraction algorithm is improved in its convergence with physics-based bounds based on the diagonally dominant structure of the impedance matrix. Embedded element patterns corrupted by noise arising both by random as well as propagation-related phenomena in a receiving system are then used to test the robustness of the method; such embedded element patterns are artificially created but the noise estimates from real on-site measurements are also used for comparison. The mutual impedance matrices extracted from the "noisy" radiation patterns at 110 and 320 MHz are accurate to within 2 to 3%. This work has direct application to the SKA-Low telescope.**

***Index Terms*—Antenna array mutual coupling, antenna radiation patterns, radio astronomy, embedded element patterns, mutual impedance matrix, UAV measurements**

I. INTRODUCTION

IN phased array antennas, the concept of the mutual impedance matrix (MIM) is very useful for describing the array properties as a network of ports, whether in a transmit or receive mode. Due to the linearity of the antenna fields, the MIM can linearly map the embedded element patterns (EEPs) to changing loading conditions at the array ports, as well as weight the inputs/outputs of a beamformer. This allows the extraction of the MIM from two sets of diversely terminated EEPs, as an alternative to its direct simulation or measurement.

Arrays such the VHF-band Square Kilometer Array Low telescope (SKA-Low) [1] pose major challenges for direct MIM evaluation through either simulation or measurement. Their simulations incur significant computational costs, and measurements are time-consuming due to the numerous ports involved and their deployment in very remote locations in harse environments. Each full SKA-Low "station" comprises 256 dual-polarised log-periodic antennas arranged in an aperiodic configuration. Each station is discretised by a mesh of approximately 10^6 degrees of freedom. SKA-Low is planned to consist of 512 such stations. The focus of this paper is to derive the MIM for one of the earlier technology demonstrator prototype arrays called the Aperture Array Verification System 1.5 (AAVS1.5), deployed in 2019.

The AAVS1.5 [2] served as an intermediary prototype in the progression towards constructing the subsequent precursor AAVS2.0 [3]. Both prototypes were constructed to verify engineering functionality, sensitivity, the ability to create calibration solutions, as well as other SKA-Low requirements, such as beamforming and polarization [4]. AAVS1.5 was the first prototype to use SKALA4.1 as an antenna element [5] deployed on a 38 m diameter circular ground plane at the Murchison Radioastronomy Observatory (MRO). It was comprised of three 16-antenna clusters, each arranged in a quasi-random configuration, as shown in Fig. 1 [6]. Quasi-random arrays are preferred in wide-band aperture arrays for radio astronomy to avoid grating lobes at station level, and provide overall array-level pattern diversity for inter-station interferometric imaging. The proposed quasi-random antenna locations were adjusted to satisfy the physical accessibility requirement for future maintenance. In this paper, for simplicity, we focus only on the Cluster 1, ignoring the other two clusters. Shortly after completion of the UAV measurement campain, AAVS1.5 was expanded to become AAVS2.0.

The motivation of this research is to verify that the mutual impedance matrix extraction (MIME) technique is accurate for *in situ* validation. Following deployment of AAVS1.5, electromagnetic simulations of the EEPs were verified via unmanned aerial vehicle (UAV) measurements. The comparison between simulated and measured EEPs was presented in [7]. These results are applied in our modelling in Sec. IV-C1. The use of measured EEPs does not only aim at characterising the station's performance, but have been proposed to assist advanced calibration routines [8]. Similarly, knowledge of the actual, as-deployed array impedance matrix would provide important confirmation of simulation results, as might also find use in various telescope models [9]. Obtaining the impedance matrix through on-site measurements is a challenging task, exacerbated by the physical scale of the array and the instrumental requirements (including cables and VNA calibration)

Manuscript received May 07, 2024. This work was supported by the Government of Western Australia. The first two authors contributed equally to this work. *(Corresponding author: Maria Kovaleva)*

M. Kovaleva and D. Davidson are with the International Centre for Radio Astronomy Research (ICRAR-Curtin), Curtin University, 1 Turner Avenue, Bentley, WA 6102, Australia (e-mail: maria.kovaleva@curtin.edu.au)

G. Kyriakou and P. Bolli are with INAF-Arcetri Astrophysical Observatory, Largo Enrico Fermi 5, 50125, Florence, Italy (e-mail: georgios.kyriakou@inaf.it)

K. F. Warnick is with the Department of Electrical and Computer Engineering, Brigham Young University, Provo, UT 84602 USA (e-mail: warnick@ee.byu.edu)

in a harsh MRO environment. It may well turn out to not be feasible.

The first objective of this work is to extend the scope of the MIM extraction algorithm to larger arrays. The second objective is to obtain the mutual impedance matrix (MIM) for Cluster 1 of the AAVS1.5 array from EEP measurements and compare it with the simulated MIM, as well as provide the estimates of a potential error in the extraction procedure. Sec. II describes the theoretical groundwork of MIM extraction. Sec. III introduces new physics-driven improvements to the algorithm and examines a simple isotropic radiator array. Sec. IV presents these results for simulated and mock-measurement patterns. This has been achieved by developing a noise model for generating "measured" EEPs and performing Monte-Carlo simulations of MIM extraction. Finally, Sec. V outlines our conclusions.

II. Transforming EEPs for Different Loads

A. EEP transformations under arbitrary loads and the fixed Thevenin source case

Since Kelley's original work [10], it has been known that the relationship between embedded element patterns and a mutual impedance $\mathbf{Z}_A$ (or admittance $\mathbf{Y}_A$) matrix of an array is described by microwave network theory. Pattern transformation between various loading conditions of the array have also been thoroughly described in [11]. However, these derivations only considered simple cases where the loading condition is the same for all array elements, including the ones excited. Recently, in [12], it was shown that this is only practical for electromagnetic simulations, whereas in EEP measurements, a transmitter or receiver (a fixed Thevenin source, in network representation) has a fixed generator impedance not necessarily equal to the impedance of the loads attached to the array elements (which is, typically, a low-noise amplifier impedance in receiving arrays).

Let us begin by introducing the simple case of antennas loaded by an impedance $Z_{\mathrm{L1}} = Z_{\mathrm{g1}}$, which is the same as the generator internal impedance Z_{g1} used for their successive excitation. Then, one can transform the EEPs to another loading condition $Z_{\mathrm{L2}} = Z_{\mathrm{g2}}$ by computing:

$$\mathbf{E}^{\mathbf{Z}_{L2}} = (\mathbf{Z}_A + \mathbf{Z}_{L2})^{-\mathrm{T}} (\mathbf{Z}_A + \mathbf{Z}_{L1})^{\mathrm{T}} \mathbf{E}^{\mathbf{Z}_{L1}} \tag{1}$$

where $\mathbf{Z}_{L1} = Z_{L1}\mathbf{I},\ \mathbf{Z}_{L2} = Z_{L2}\mathbf{I}$. It is also useful to repeat here the cases where one of the two conditions is either open-circuit (oc) or short-circuit (sc) since these are special cases of theoretical interest for an array. We have:

$$\mathbf{E}^{\mathrm{oc}} = \mathbf{Z}_A (\mathbf{Y}_A + \mathbf{Y}_{\mathrm{L1}})^{\mathrm{T}} \mathbf{E}^{\mathbf{Z}_{L1}} \tag{2}$$

$$\mathbf{E}^{\mathrm{sc}} = \mathbf{Y}_A^{\mathrm{T}} (\mathbf{Z}_A + \mathbf{Z}_{\mathrm{L1}})^{\mathrm{T}} \mathbf{E}^{\mathbf{Z}_{L1}} \tag{3}$$

One point that needs to be clarified is that while the short-circuit expression is found by directly substituting $\mathbf{Z}_{\mathrm{L2}} = 0$, the open-circuit condition clearly cannot employ the same generator and loading impedance, since that is essentially infinite. The given expression takes into account a current generator, and is derived by the dual representation of the network by admittances.

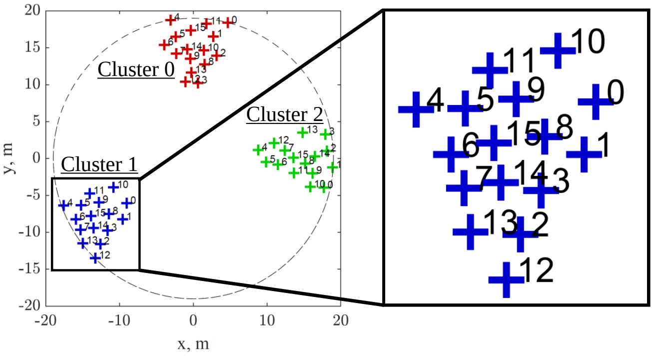

Fig. 1. Aperture Array Verification Station 1.5 with a zoom-in image of Cluster 1.

The practical implications of using the same generator and load impedance are apparent when we use a fixed transmitter. This has prompted the question of whether a general expression exists that would connect different sets of EEPs when the generator impedance is fixed. As shown in [12], such an equation can be calculated as:

$$\mathbf{E}^{\mathrm{sc}} = \mathbf{Y}_A^{\mathrm{T}} (\mathbf{Z}_A + \mathbf{Z}_{\mathrm{L1}})^{\mathrm{T}} \mathbf{F} \mathbf{E}^{\mathbf{Z}_{L1},\mathrm{th}} \tag{4}$$

where $\mathbf{F}$ is a diagonal matrix with diagonal entries $[\mathbf{F}]_{nn} = 1 + (Z_g - Z_{\mathrm{L1}})[(\mathbf{Z}_A + \mathbf{Z}_{\mathrm{L1}})^{-1}]_{nn}$. These expressions simplify to more compact ones when $\mathbf{Z}_{\mathrm{L1}}$ corresponds to oc and sc conditions:

$$\mathbf{E}^{\mathrm{sc}} = Z_0 \mathbf{Y}_A^{\mathrm{T}} (\mathbf{I} + Y_0 \mathbf{Z}_{A,d}) \mathbf{E}^{\mathrm{oc,th}} \tag{5}$$

$$\mathbf{E}^{\mathrm{sc}} = (\mathbf{I} + Z_0 \mathbf{Y}_{\mathrm{A,d}}) \mathbf{E}^{\mathrm{sc,th}} \tag{6}$$

where $Z_0,\ Y_0$ are the reference impedance and admittance, respectively. Combining Eqs. (5), (6) one derives:

$$\mathbf{E}^{\mathrm{oc,th}} = Y_0 (\mathbf{I} + Y_0 \mathbf{Z}_{\mathrm{A,d}})^{-1} \mathbf{Z}_A (\mathbf{I} + Z_0 \mathbf{Y}_{\mathrm{A,d}}) \mathbf{E}^{\mathrm{sc,th}} \tag{7}$$

where $\mathbf{Z}_{A,d},\ \mathbf{Y}_{A,d}$ denote the diagonal respective matrices. This is a non-linear equation that cannot be inverted for $\mathbf{Z}_A$. Instead, numerical routines have to be employed for its solution, with iterative methods being the preferred ones. In these methods, starting from an initial guess $\mathbf{Z}_{A,0}$, one can compute $\mathbf{E}_0^{\mathrm{oc,th}}$ and compare it to $\mathbf{E}^{\mathrm{oc,th}}$. A correction is then applied to $\mathbf{Z}_{A,0}$ and the procedure is repeated n_{iter} times until $\mathbf{E}_{n_{iter}}^{\mathrm{oc,th}} \rightarrow \mathbf{E}^{\mathrm{oc,th}}$. This convergence is usually expressed by a goal function $G(\cdot)$ that the routine tries to minimize or find the matrix $\mathbf{Z}_{A,n_{iter}}$ such that $G(\mathbf{Z}_{A,n_{iter}}) \rightarrow 0$.

III. MIM Extraction Method Adapted for Large Aperiodic Arrays

A. Goal function and optimization space bounds

The goal function is an important aspect of an optimization routine defining its convergence rate. In this study, as in [12], the goal function G was defined as a relative error of the optimization result with respect to the ground-truth quantity:

$$G(\hat{\mathbf{Z}}_A) = \frac{||\mathbf{E}^{\mathrm{oc,th}} - \mathbf{A}(\hat{\mathbf{Z}}_A)\mathbf{E}^{\mathrm{sc,th}}||}{||\mathbf{E}^{\mathrm{oc,th}}||} \tag{8}$$

where

$$\mathbf{A}(\hat{\mathbf{Z}}_A) = Y_0(\mathbf{I} + Y_0\hat{\mathbf{Z}}_{A,d})\hat{\mathbf{Z}}_A^{-1}(\mathbf{I} + Z_0\hat{\mathbf{Y}}_{A,d}) \tag{9}$$

and $\hat{\mathbf{Z}}_A$ denotes an estimation of $\mathbf{Z}_A$. The EEPs $\mathbf{E}^{\mathrm{oc,th}}$, $\mathbf{E}^{\mathrm{sc,th}}$ can be simulated or measured patterns.

Common matrix norms include the 2-norm $||\mathbf{M}||_2 = \sqrt{\lambda_{\max}(\mathbf{M}^H\mathbf{M})}$ (where $\lambda_{max}(\cdot)$ is the maximum eigenvalue) and the Frobenius norm $||\mathbf{M}||_F = \sqrt{\mathrm{Tr}(\mathbf{M}^H\mathbf{M})}$. In our case, the impedance matrix $\mathbf{Z}_A$ has some special structure. Due to the fact that most elements are separated at distances that are several wavelength multiples in electrical length, a diagonally dominant matrix structure is a characteristic of $\mathbf{A}$, as is also for $\mathbf{Z}_A$, as can bee seen in Fig. 2. Initial attempts with the 2-norm were proven to bias the optimization procedure; indeed, this norm does not take into account the full spectral decomposition of a matrix by retaining the largest effect across principal directions, which for diagonally dominant matrices is an eigenvalue strongly bounded by the diagonal elements' values [13]. Therefore, w choose the Frobenius norm which is a more intuitive metric, ultimately expressed as a sum of squares and which can be recast in a uniform sum of spectral components, as it is rotationally invariant.

An important improvement that we can achieve in our search space in order to avoid converging to non-physical solutions of (7) is to restrict each matrix element using theoretical information on the impedance value bounds.

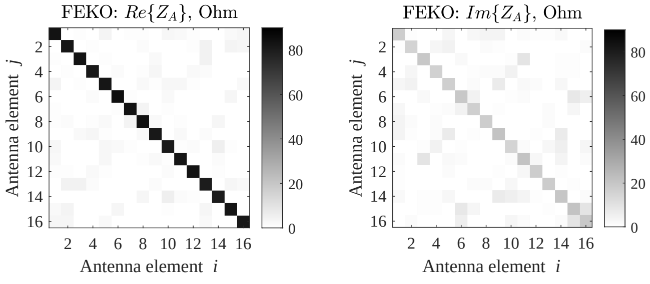

(a) 110 MHz

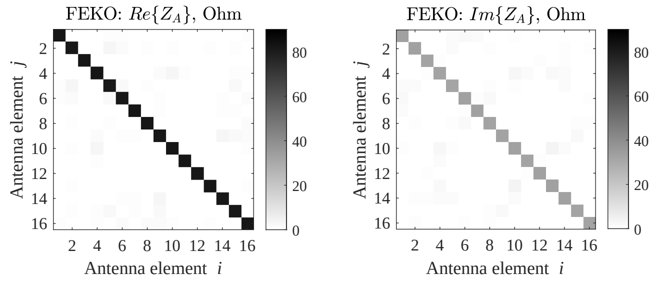

(b) 320 MHz

Fig. 2. Element-wise display of the real and imaginary components of the benchmark $\mathbf{Z}_A$ obtained from FEKO demonstrates the diagonal dominance of the matrix at (a) 110 MHz and (b) 320 MHz.

Following [14], in an array of identical elements:

1) The self-impedances, $Z_{11}, \ldots, Z_{NN}$ are all approximately equal to the impedance of the isolated element Z_{iso} when the edge effects are ignored [14, Ch. 4.8.4]. In a large array, the lateral elements are the ones suffering edge effects, but as the radius of the circle which encompasses the array gets larger, the less severe these effects become [15, Ch. 6.5]. In our case, we are going to assume that for all $n = 1, \ldots, N: \ Z_{nn} \in [Z_{\mathrm{iso}} - \Delta Z,\ Z_{\mathrm{iso}} + \Delta Z]$.
2) The mutual impedances $Z_{ij},\ i \neq j$ depend on the distance between the elements. If the elements were isotropic, then [14, Ch. 4.8.5]: $\Re\{Z_{ii}\} = 2P_{\mathrm{rad}}/|I_0|^2$ and $\Re\{Z_{ij}\} = 2P_{\mathrm{rad}}/|I_0|^2\mathrm{sinc}(kR_{ij}) = \Re\{Z_{ii}\}\mathrm{sinc}(kR_{ij})$, where I_0 is the current excitation for the calculation of open-circuit EEPs and P_{rad} the isotropically radiated power. We can therefore calculate similar bounds for the mutual resistance by multiplying the real self-resistance by the factor $\mathrm{sinc}(kR_{ij})$, where k is the wavenumber and R_{ij} is the physical distance between elements $i,\ j$. Even though this is not strictly true for the mutual reactance, Vendik et. al. [16] have shown that by the Kramer-Kronigs relationship a similar functional dependence can describe the reactance, thus we will use the same bounds for it too. To allow for strong coupling that exceeds the isotropic radiator theoretic bounds, we can grow these bounds by a factor g. We will choose a $g \approx 2$.

Our criterion to ascertain the validity of the resulting matrix in the numerical optimization performed is the relative error, calculated as:

$$\Delta\mathbf{Z}_A = \frac{||\mathbf{Z}_A - \hat{\mathbf{Z}}_A||_F}{||\mathbf{Z}_A||_F} \tag{10}$$

where $\mathbf{Z}_A$ is the ground-truth antenna matrix (always simulated), and $\hat{\mathbf{Z}}_A$ is the estimated matrix by the optimization routine. Throughout this paper, $\Delta\mathbf{Z}_A$ is presented in percentage if not stated otherwise.

B. Example: Isotropic radiators

As a verification example, we examine the case of an array of isotropic radiators, which helps in establishing convergence properties. This is because the isotropic radiator does not present directive characteristics, which would create irregularly populated matrices of far-field points, while at the same time it does not discriminate between co- and cross-polarized patterns. For comparison purposes, we will use 16 ideal radiators of the bent $\lambda/4$ isotropic dipole [17], placed at the same positions as those of the AAVS1.5 layout. The pattern of this radiator can be written in an analytic form, which allows us to calculate the mathematical limit when the joint of the two monopoles (where the port is also defined) is infinitesimaly small, thus approaching the isotropic radiation condition. This is preferable to simulating other types of quasi-isotropic radiators for which the limits might only be approached numerically.

The results obtained in this section use the theoretic formulas for the computation of both the Thevenin-source referred

EEPs as well as the impedance matrix. The mutual coupling effects are first-order, due to the minimum scattering nature of the antenna under test which imparts only phase perturbations of the isolated element pattern [14, Ch. 4]. Therefore, we phase-shift the isotropic element pattern to form the EEPs and use the power conservation to compute the real part of the impedance matrix. The mutual reactances are computed according to [18], while we also assume self-resonancy at the frequency tested, that is zero self-reactances.

In Fig. 3, we report the relative error by using the improvements introduced in Sec. III-A. We examine 37 diverse sampling scenarios, and four distinct strategies for the sampled quantities: either only the co-polar electric far-field is sampled, or both the co-polar and cross-polar fields, while in each of those choices, either the same ϕ-planes are examined, or two ϕ-planes that are 90° apart. The θ sampling is retained to 0.5° from -90° to 90°. Some ϕ cuts (0° or 90°) are not shown since the respective electric field component is zero and the problem is ill-defined. It is evident from these curves that the only strategy that leads to converged $\mathbf{Z}_A$ recovery is sampling both the polarization components, at plane cuts that are 90° apart. This is the strategy we adopt in the next section.

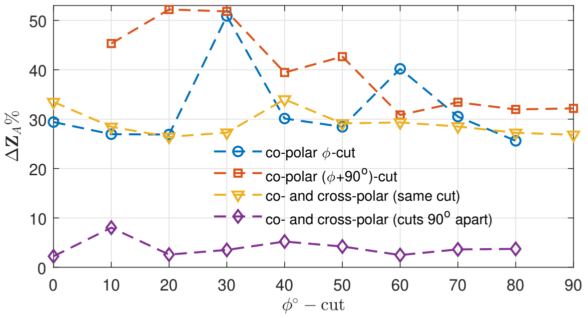

Fig. 3. Relative error $\Delta\mathbf{Z}_A$ for a 16-element array of isotropic U-shaped radiators for different sampling strategies, both in terms of polarization and ϕ-cuts.

IV. MIM EXTRACTION RESULTS FOR AAVS1.5

A. *Simulated EEPs*

We applied the MIM extraction on simulated EEPs of the AAVS1.5 Cluster 1 at 110 and 320 MHz, which were carried out using the method of moments in FEKO, while (5), (6) are used for the trasformation to the Thevenin-source referred open-circuit and short-circuit EEPs. In the simulation, all 16 antennas were terminated with $Z_L = Z_g = 50\ \Omega$, the other two clusters were omitted, and the size of the perfect electric conductor ground plane was considered infinite. The EEPs that we used in this study are for north-south (Y)-polarization and correspond to the E-plane (ϕ-component) pattern of the resulting far-fields. Initially, we used a dense uniform hemisphere coverage with a θ step of 0.5° ($M = 361$ points) within $\theta \in [-90^\circ, 90^\circ]$, and later, we showed that an accurate MIM extraction can be obtained even for $\theta \in [-45^\circ, 45^\circ]$ with a coarse field sampling. The S-parameter matrix was also simulated in FEKO and transformed to $\mathbf{Z}_A = Z_0(\mathbf{I}-\mathbf{S})^{-1}(\mathbf{I}+\mathbf{S})$, which will be used as the ground-truth quantity for the comparison with the extracted $\hat{\mathbf{Z}}_A$.

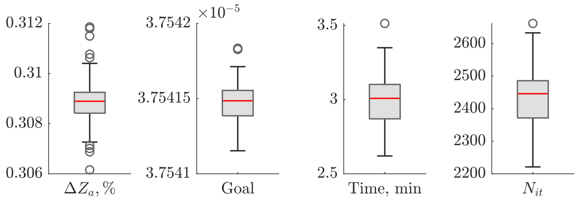

(a) 110 MHz

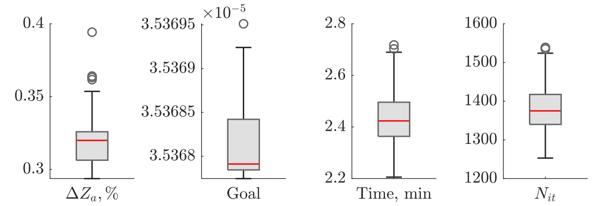

(b) 320 MHz

Fig. 4. Box and whiskers plots show statistical indicators of 100 Monte-Carlo runs for $\Delta\mathbf{Z}_A$ (10), goal function (8), overall extraction time in minutes and number of iterations. Red lines show mean values. The EEPs contained $M = 361$ samples within $\theta \in [-90^\circ, 90^\circ]$.

As an optimization routine, MATLAB's `fmincon` was used since it can easily handle the bounds outlined in Sec. III-A. The number of independent complex unknowns in a mutual impedance matrix for $N = 16$ antennas is N^2, and since both real and imaginary components are independent, the total number of variables is $2N^2$. However, due to reciprocity, it is only necessary to find the upper triangular matrix, which reduces the total number of unknowns to $N(N+1)$. The optimisation is initialised with a uniform random sampling from the respective bounds of diagonal and off-diagonal elements. At 110 MHz, the self-impedance (which we take the same as the isolated antenna impedance Z_{iso}) is $Z_{\text{iso}} = 82 + j18.3\ \Omega$, $\Delta Z = 20\ \Omega$, and at 320 MHz, $Z_{\text{iso}} = 80 + j30\ \Omega$, $\Delta Z = 20\ \Omega$. To analyse the stability of the MIM extraction procedure, we implemented the Monte-Carlo method.

Fig. 4 presents box-and-whiskers diagrams for the MIM extraction of 100 Monte-Carlo runs at 110 and 320 MHz. The graph contains median values (red horizontal line), the interquartile range (box) and min/max bounds (whiskers). Apart from $\Delta\mathbf{Z}_A$, we also show the goal function value, total running time and number of iterations for the `fmincon` routine. The key information from Fig. 4 is that the average error in MIM extraction is approximately 0.3% at either frequency, and the procedure of obtaining $\hat{\mathbf{Z}}_A$ takes 2-3 mins, which is computationally inexpensive.

Fig. 5 shows the element-wise relative error for all the 16×16 matrix elements as pixels, both in amplitude and phase. As can be seen, the majority of amplitude errors are $\leq 0.5\%$, which is very small, with the exception of some symmetric entries among which the highest is 2.3%. We noticed that the highest relative errors occur at the entries with low absolute values. The error in phase is also very low, below 1.2°.

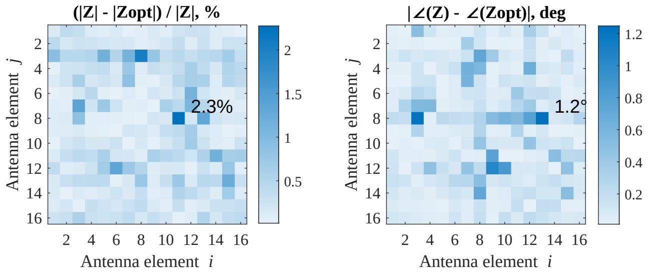

Fig. 5. 320 MHz. Element-wise relative percentage magnitude difference and absolute phase difference (in deg) between mean reconstructed $\hat{\mathbf{Z}}_A$ over 100 Monte-Carlo runs and the benchmark $\mathbf{Z}_A$ obtained from FEKO. The EEPs contained $M = 361$ samples within $\theta \in [-90°, 90°]$.

B. Simulated EEPs Truncated to the Field of View of the Array

While a very low relative error is obtained for the simulated EEPs sampled with a $0.5°$ step in an entire upper hemisphere for $\theta \in [-90°, 90°]$, it is of practical importance to consider the simulated EEP values only within the a more restricted field of view — for SKA-Low, a cone with half-angle $45°$ from zenith. In an UAV measurement campaign [7], only the angular coverage in this cone was captured with high fidelity.

The same procedure as described in Sec. IV-A was applied to truncated EEPs ($\theta \in [-45°, 45°]$) with dense field samples (θ step is $0.5°$, $M = 181$ points), and $\Delta\mathbf{Z}_A$ was extracted. Since the MIM extraction procedure has been proven to have low statistical deviations, the Monte-Carlo method with $n = 10$ runs was performed to reduce the overall computation time. Fig. 6 shows that while there is an increase in $\Delta\mathbf{Z}_A$, the error still remains under 1% with an exception of one entry with $\approx 11\%$ error in amplitude and $\approx 3°$ error in phase. The absolute value of this mutual impedance entry is at the same time within the lowest values of the array. This is an indication of the fact that the algorithm might be more influenced by the relative error of the highest matrix entries.

For the purpose of understanding how the MIM extraction procedure is affected by the number of field samples, we took EEPs within $\theta \in [-45°, 45°]$ and varied the number of field points $\{M_1, M_2, ..., M_{11}\}$, as shown in Fig. 7. To avoid creating an underdetermined problem, the minimum number of required EEP points must be equal to the number of variables per equation. For (7), this is $\min(M) = 272/32 = \text{round}(8.5) = 9$. Considering our simulated θ grid, the minimum number of field samples is $M_1 = 10$ points.

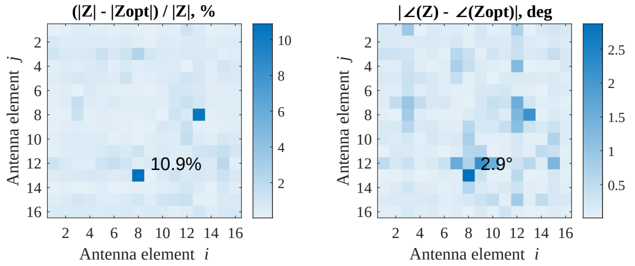

Fig. 6. 320 MHz. Element-wise relative percentage magnitude difference and absolute phase difference (in deg) between mean reconstructed $\hat{\mathbf{Z}}_A$ over 10 Monte-Carlo runs and the benchmark $\mathbf{Z}_A$ obtained from FEKO. The EEPs contained $M = 181$ samples within $\theta \in [-45°, 45°]$.

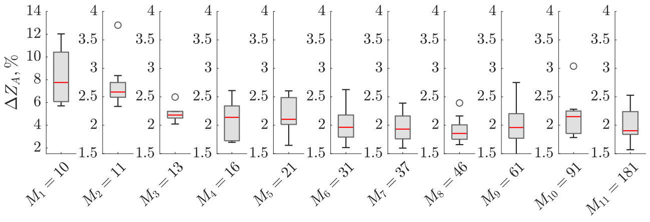

(a) 110 MHz

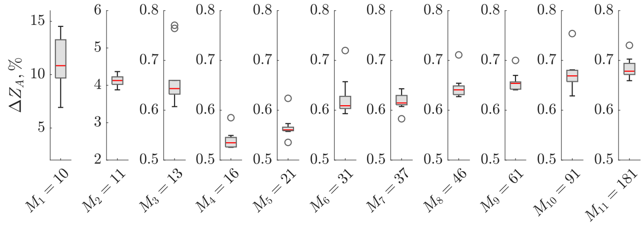

(b) 320 MHz

Fig. 7. Relative error of $\mathbf{Z}_A$ for M sample points in EEP data: (a) 110 MHz and (b) 320 MHz. Box and whiskers plots show the statistical indicators of 10 Monte-Carlo runs. EEPs are within the field of view, $\theta \in [-45°, 45°]$.

Fig. 7 shows the statistics of 10 Monte-Carlo runs for the relative error (10) of MIM extraction for 110 and 320 MHz as a function of field samples in EEPs. It can be seen that the mean error and its standard deviation is much higher for 10 points, but starting from $13 - 16$ points, the error takes its lowest value, and oversampling the EEPs does not bring further improvement. This is an important conclusion that has not been previously shown. Another point to note is that at 110 MHz, the average $\Delta\mathbf{Z}_A \approx 2.6\%$, is slightly higher than at 320 MHz, which is $\Delta\mathbf{Z}_A \approx 1.9\%$. The reason for this is the truncated EEPs. Before truncation, $\Delta\mathbf{Z}_A$ was $\approx 0.3\%$ (Fig. 4). It will be seen in Sec. IV-C that at lower frequency, since the half-power beamwidth is wider, truncating EEPs to $\pm 45°$ causes the loss of information about side lobe levels, and the MIM extraction error increases.

C. EEPs Corrupted by Measurement Noise

1) EEP Measurement Noise Model: For electrically large antenna arrays such as the SKA-Low, the only viable measurement practice is the field measurement rather than using an anechoic chamber. Such measurements are performed by unmanned aerial vehicles (UAVs) carrying a transmitter, whereas the received signal is sent from the antennas to a spectrum analyzer. For the AAVS1.5 station prototype, a campaign performed on the grounds of the MRO in 2019 measured the amplitude and phase of embedded element patterns for 3 clusters of 16 SKALA4.1 antennas each, a subset of the 256 antennas of one SKA-Low station (these clusters are now part of AAVS2.0). In these measurements, root-mean-square (RMS) discrepancies between simulations and measurements are reported, providing the statistics of the additive white noise. Furthermore, gain equalization was performed on the measured data separately for each antenna free-space and receiver channel with corresponding uncertainties, which emulate multiplicative noise.

While UAV-measurements of AAVS1.5 were conducted, antennas were terminated with low-noise amplifiers (LNAs) with $Z_L = 50\ \Omega$ and thus, $\mathbf{E}^{\mathbf{Z}_L}$ patterns were measured. Since antennas could not be terminated with short-circuit and open-circuit loads for the UAV campaign, $\mathbf{E}^{\mathrm{sc,th}}$ and $\mathbf{E}^{\mathrm{oc,th}}$ required for the MIM extraction were not obtained. Therefore, it was necessary to develop a model that would represent measured $\mathbf{E}^{\mathrm{sc,th}}$ and $\mathbf{E}^{\mathrm{oc,th}}$ taking information about measurement uncertainties from measured $\mathbf{E}^{\mathbf{Z}_L}$.

Any noise-free signal $\mathbf{x}$ can generally be corrupted by additive ($\mathbf{n}$) and multiplicative ($\mathbf{G}$) noise and converted to a noisy signal $\mathbf{y}$ as:

$$\mathbf{y} = \mathbf{G}\mathbf{x} + \mathbf{n} \tag{11}$$

In our case, $\mathbf{G}$ is a diagonal matrix of random variables describing channel gains (no crosstalk) and $\mathbf{n}$ is a vector describing the additive white noise. As known from random noise theory [19], a multiplicative channel response on the amplitude of a signal with a strong line-of-sight component (the free path loss in [20]) is modelled by a Rician distribution $\mathcal{R}(\nu, \sigma_R)$, while the white noise is modelled by a Gaussian distribution $\mathcal{N}(0, \sigma_N)$.

To find the parameters of each distribution, we used the measurement data presented in [7], [21] and extracted statistical properties following the steps below:

- Calculate equalization gains by enforcing a zero mean on $\mathbf{n}$ of (11). That way, $g_n = \mathbb{E}_\theta\{y_n\}/\mathbb{E}_\theta\{x_n\}$. The RMS of $\mathbf{n}$ over all θ and $N = 16$ antenna channels is then an estimate $\hat{\sigma}_N$ of σ_N.
- Take the mean $\hat{\mu}_R$ and RMS $\hat{\sigma}_R$ of $\mathbf{g} = [g_1 \dots g_N]$ across all $N = 16$ antenna channels to extract the Rician distribution parameters (ν, σ_R) using well-known fitting processes from the literature [22]. We used `fitdist` from MATLAB.

In [7], most of the gain level discrepancies were compensated for the various known contributions to the receiving chain, which include the receiver and transmitter gains, cable losses, as well as mismatch and insertion losses [20]. In this paper, we used the raw measured data without these corrections. Therefore, our relative error results are the upper limits of the accuracy that can be achieved for MIM extraction using measured EEPs. Table I presents parameters $\hat{\sigma}_N$, $\hat{\mu}_R$, $\hat{\sigma}_R$ at 110 and 320 MHz as extracted from the measurement data in [7].

The matrix extraction method, as can be confirmed by (7), is independent of the amplitude scale of the EEPs. Furthermore,

TABLE I
σ VALUES OF GAUSSIAN AND RICIAN DISTRIBUTIONS FROM UAV EEP MEASUREMENTS OF AAVS1.5

f (MHz)/Pol.	110/X	320/X	110/Y	320/Y
$\hat{\sigma}_N$	0.055	0.086	0.06	0.097
$\hat{\mu}_R$	0.507	0.104	0.74	0.3
$\hat{\sigma}_R$	0.14	0.031	0.171	0.063

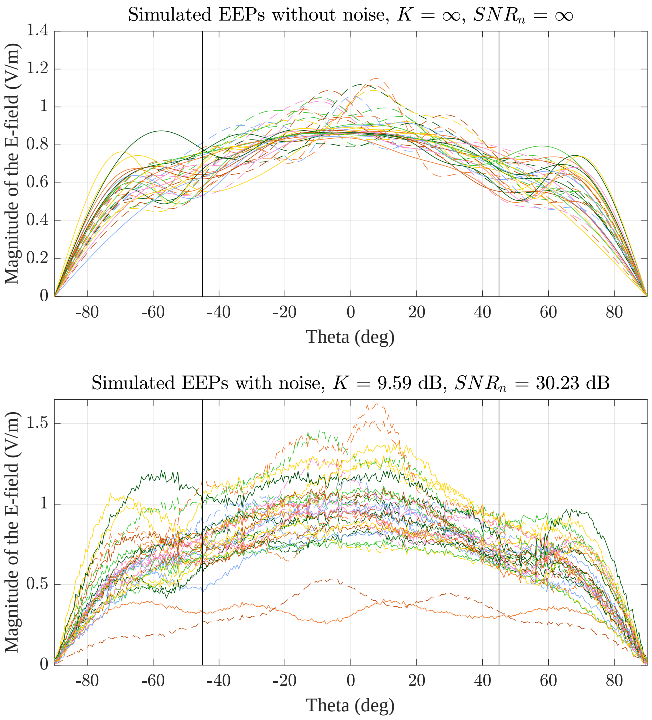

Fig. 8. 110 MHz. Open circuit and short circuit EEPs: (top) no noise, (bottom) with UAV measurement noise of $(K, \mathrm{SNR}_\mathbf{n}) = (9.59,\ 30.23)$ dB. For the MIM extraction, these EEPs were truncated to $\theta \in [-45°, 45°]$, $M = 181$ samples (vertical black lines).

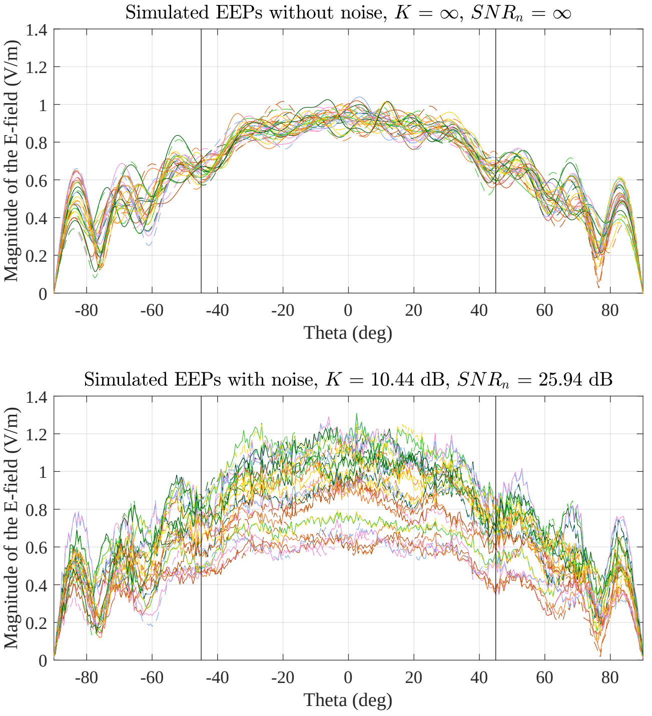

Fig. 9. 320 MHz. Open circuit and short circuit EEPs: (top) no noise, (bottom) with UAV measurement noise of $(K, \mathrm{SNR}_\mathbf{n}) = (10.44,\ 25.94)$ dB. For the MIM extraction, these EEPs were truncated to $\theta \in [-45°, 45°]$, $M = 181$ samples (vertical black lines).

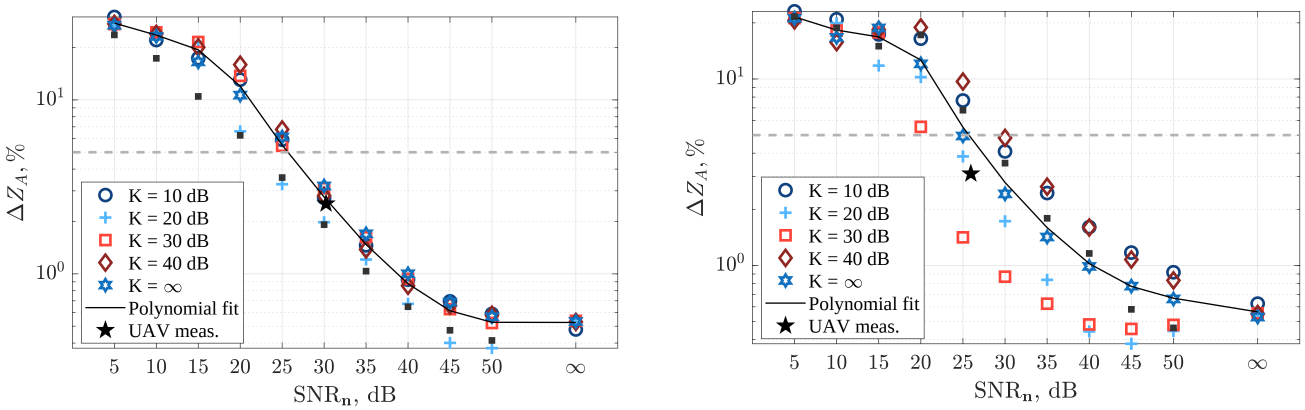

(a) 110 MHz

(b) 320 MHz

Fig. 10. $\Delta\mathbf{Z}_A$ for the noise-modelled EEPs ($\theta \in [-45°, 45°]$, $\Delta\theta = 0.5°$, $M = 181$ points) over 10 Monte-Carlo runs: (a) 110 MHz, (b) 320 MHz. $\mathrm{SNR}_{\mathbf{n}}$ represents additive noise modelled as random Gaussian variables. K represents multiplicative noise modelled as Rician random variables. Small black square markers show $\Delta\mathbf{Z}_A$ for $K = \infty$, $M = 361$ field samples, $\theta \in [-90°, 90°]$.

note that our equalizing gains do not exactly coincide with the gain calculations of [7], even though we are using the same measured data; a reference antenna is used there for more robust calibration effectively scaling the system response to a desired gain level well characterized by independent measurements. Thus, scaling of the gains to a mean value of $\hat{\mu}_R = 1$ (which, for small $\hat{\sigma}_R$ means $\nu = 1$) simplified our implementation routines without affecting the resulting $\mathbf{Z}_A$ matrix or violating the measurement practice which the noise modelling is based on.

2) Results: We simulated various implementations of the noise model described by (11) in Sec. IV-C1 by varying both additive and multiplicative noise. Standard statistical parameters were used in order to characterize each implementation: (1) for the multiplicative noisy gains $\mathbf{G}$, 16 channel gains $\mathbf{g}$ define a factor called $K = \frac{\nu^2}{2\sigma_R^2}$ in Rice distributions (representing the "fading" level in telecommunications [23]), (2) when the additive noise is included, the instantaneous signal-to-noise ratio is defined in our notation as $\mathrm{SNR}_{\mathbf{n}} = \frac{1}{N}\frac{\mathbb{E}_\theta\{||\mathbf{Gx}||^2\}}{\hat{\sigma}_N^2}$. For all combinations of $K \in \{10,\ 20,\ 30,\ 40\}$ dB and $\mathrm{SNR}_{\mathbf{n}} \in \{5,\ 10,\ \ldots,\ 50\}$ dB, random $\mathbf{G}$ and $\mathbf{n}$ were generated and applied to simulated EEPs, which were then used to compute the relative error for all noise combinations.

Simulated EEPs were used to create "noisy" EEPs using (11), while the same noise instance is assumed for both the OC and SC EEPs. This is of practical importance only for the fading factor, and we assume a slowly fading channel with coherence time much longer than the acquisition of two mock measurements. Fig. 8 and Fig. 9 show OC and SC EEPs for all 16 antenna elements first without noise (FEKO-simulated EEPs) and then, with the UAV measurement noise model for 110 MHz and 320 MHz, respectively. It can be seen that the patterns of two antenna elements are significantly attenuated; this is attributed to the outlier values of the 16-sampled instances of the random variables g. The same procedure as described in Sec. IV-A was applied to truncated "noisy" high-resolution EEPs ($\theta \in [-45°, 45°]$, $\Delta\theta = 0.5°$, $M = 181$ points), and the MIM extraction algorithm was repeated 10 times for each $(K, \mathrm{SNR}_{\mathbf{n}})$ pair to ensure statistical stability.

Fig. 10a and Fig. 10b show the mean percentage relative error for 110 and 320 MHz, respectively. Fig. 10 is the main result of this paper. Infinite $\mathrm{SNR}_{\mathbf{n}}$ and K simply mean the absence of additive or multiplicative noise, and therefore, their respective random variables were substituted by their deterministic values $n = 0$ or $g = 1$. A horizontal grey line marks the desired error threshold of 5% relative error[1]. From UAV-measured EEPs of AAVS1.5 Cluster 1, at the first frequency of interest, $\Delta\mathbf{Z}_A = 2.5\%$, which is displayed at $(K, \mathrm{SNR}_{\mathbf{n}})$@110 MHz $= (9.59,\ 30.23)$ dB and at the second frequency, $\Delta\mathbf{Z}_A = 3.1\%$, which is shown at the point $(K, \mathrm{SNR}_{\mathbf{n}})$@320 MHz $= (10.44,\ 25.94)$ dB. If UAV measurements could have been obtained in $\theta \pm 90°$ with $M = 361$, $\Delta\mathbf{Z}_A$ would decrease to 1.2% at 110 MHz and to 1.6% at 320 MHz. Since it is not feasible to measure beam patterns in the entire hemisphere in the field, efforts should be made to increase the SNR of UAV measurements.

From Fig. 10, we observe that $\Delta\mathbf{Z}_A \le 5\%$ for $\mathrm{SNR}_{\mathbf{n}} \ge 25$ dB, which is consistent with the previous findings for dipole antennas [24]. The main advancement here are the estimates of $\Delta\mathbf{Z}_A$ for different measurement conditions taking into account both additive and multiplicative noise. Our analysis reveals that a MIM can be extracted with 10% accuracy even from the EEPs strongly corrupted by noise, such as $\mathrm{SNR}_{\mathbf{n}} = 15$ dB. It is found that the increase in additive noise increases $\Delta\mathbf{Z}_A$ linearly, while multiplicative noise changes $\mathbf{Z}_A$ in a nonlinear fashion. In that particular case, there can be EEP realisations of higher K that perform worse than that of lower K counterparts. A polynomial fitting averages the effect of the multiplicative noise, giving an estimation of the expected relative error over all possible fading levels. It is important to mention that the resulting mutual impedance matrices do not need re-scaling with a complex scale factor α that was introduced in [12] to overcome the ambiguity issue stemming from transformation insensitivity to self-impedances.

---

[1] This corresponds to less than 5 Ω in self impedance, which is typically also the level of accuracy of simulations with commerical solvers.

V. CONCLUSION

This paper advances the technique proposed in [12] and uses data obtained during UAV measurements of AAVS1.5 Cluster 1, which is an early prototype of the low-frequency component of the future largest radio astronomy observatory in the world — the SKA. We first verified the MIM extraction technique on FEKO-simulated data. The number of unknowns in the optimization problem was 272, which is much higher than in [12] or [24]. For this reason, we introduce some physical bounds in the algorithm search space. The verification was conducted at two frequencies, 110 and 320 MHz, to evaluate the accuracy of the MIME technique in both dense and sparse regimes of array operation. We relied on Monte-Carlo statistics to report the errors in MIM estimation. When simulated EEPs were used, the relative error was $0.3-0.4\%$ at both frequencies (Fig. 4). When simulated EEPs were truncated to a practical field of view of UAV measurement and the number of field samples was reduced, the mean error increased to $2-3\%$, with the mimimum and maximum error of 0.55% and 10%, respectively (Fig. 7). For UAV-measured EEPs, the relative error of MIME is also $2-3\%$ (Fig. 10).

A few important considerations emerged from this research work. First, to obtain an unambiguous MIM solution, it seems necessary to have initial $\mathbf{Z}_A$ estimations of diagonal and off-diagonal MIM entries. One-port measurement can provide a good estimate for setting up optimisation bounds. Second, it is of practical importance to know that it is not necessary to have large number of field samples (M in EEPs) to have low extraction error, and it is possible to extract $\hat{\mathbf{Z}}_A$ accurately even for the reduced field of view, which was demonstrated for $\theta \in [-45°, 45°]$ in this work. Next, we proposed a model to convert simulated EEPs to "measured" EEPs using additive and multiplicative noise. UAV measurements served to indicate typical noise values, and the error of MIME for noisy patters can inform future applications of the method regarding the expected $\Delta\mathbf{Z}_A$. The technique described in this paper can be used to advance the future work in this field.

VI. ACKNOWLEDGEMENT

This scientific work makes use of the Murchison Radio Astronomy Observatory (MRO), operated by CSIRO. We acknowledge the Wajarri Yamatji people as the traditional owners of the Observatory site.

REFERENCES

[1] P. E. Dewdney, P. J. Hall, R. T. Schilizzi and T. J. L. W. Lazio,"The Square Kilometre Array", in Proceedings of the IEEE, vol. 97, no. 8, pp. 1482-1496, Aug. 2009, doi: 10.1109/JPROC.2009.2021005.

[2] D. B. Davidson et al., "Electromagnetic modelling of the SKA-LOW AAVS1.5 prototype," in *2019 International Conference on Electromagnetics in Advanced Applications (ICEAA)*, Granada, Spain, 2019, pp. 1032-1037, doi: 10.1109/ICEAA.2019.8879294.

[3] G. Macario et. al., "Characterization of the SKA1-Low prototype station Aperture Array Verification System 2," in *J. Astron. Telesc. Instrum. Syst.*, **8**(1) 011014 (5 January 2022), https://doi.org/10.1117/1.JATIS.8.1.011014

[4] G. Macario et al., "Intrinsic Cross Polarisation maps from all-sky observations: an initial verification of SKA-Low station polarisation response", in *Publications of the Astronomical Society of Australia (under review)*, 2023

[5] P. Bolli et al., "Test-Driven Design of an Active Dual-Polarized Log-Periodic Antenna for the Square Kilometre Array," in *IEEE Open Journal of Antennas and Propagation*, vol. 1, pp. 253-263, 2020, doi: 10.1109/OJAP.2020.2999109.

[6] T. Clavier et al., "A Global-Local Synthesis Approach for Large Non-Regular Arrays," in IEEE Transactions on Antennas and Propagation, vol. 62, no. 4, pp. 1596-1606, April 2014, doi: 10.1109/TAP.2013.2284816.

[7] F. Paonessa, L. Ciorba, G. Virone, P. Bolli, A. Magro, A. McPhail, D. Minchin and R. Bhushan, "SKA-Low Prototypes Deployed in Australia: Synoptic of the UAV-Based Experimental Results" in *URSI Radio Science Letters*, **2**, Aug. 2020

[8] S. J. Wijnholds, "Embedded Element Patterns in Hierarchical Calibration of Large Distributed Arrays", in *2020 XXXIIIrd General Assembly and Scientific Symposium of the International Union of Radio Science*, doi:10.23919/URSIGASS49373.2020.9232295

[9] A. T. Josaitis, A. Ewall-Wice, N. Fagnoni, E. de Lera Acedo, "Array element coupling in radio interferometry I: a semi-analytic approach", in *Monthly Notices of the Royal Astronomical Society*, Volume 514, Issue 2, August 2022, pp. 1804–1827

[10] D. F. Kelley, "Embedded element patterns and mutual impedance matrices in the terminated phased array environment," in *2005 IEEE Antennas and Propagation Society International Symposium*, Washington, DC, USA, 2005, pp. 659-662 vol. 3A, doi: 10.1109/APS.2005.1552340.

[11] K. F. Warnick, D. B. Davidson and D. Buck, "Embedded Element Pattern Loading Condition Transformations for Phased Array Modeling," in *IEEE Transactions on Antennas and Propagation*, vol. 69, no. 3, pp. 1769-1774, March 2021, doi: 10.1109/TAP.2020.3027593.

[12] D. Buck, K. F. Warnick, R. Maaskant, D. B. Davidson and D. F. Kelley, "Measuring Array Mutual Impedances Using Embedded Element Patterns," in *IEEE Transactions on Antennas and Propagation*, vol. 71, no. 1, pp. 606-611, Jan. 2023, doi: 10.1109/TAP.2022.3217324.

[13] J. Barlow and J. Demmel"Computing Accurate Eigensystems of Scaled Diagonally Dominant Matrices", in *SIAM Journal on Numerical Analysis*, 1990, 27**3**, pp. 762-791

[14] K. Warnick, R. Maaskant, M. Ivashina, D. Davidson and B. Jeffs, "Phased Arrays for Radio Astronomy, Remote Sensing, and Satellite Communications" (*EuMA High Frequency Technologies Series*), Cambridge: Cambridge University Press, 2018, doi:10.1017/9781108539258

[15] Robert Mailloux, "Phased Array Antenna Handbook", Third Edition, Artech, 2017.

[16] O. G. Vendik and D. S. Kozlov, "A Novel Method for the Mutual Coupling Calculation Between Antenna Array Radiators: Analysis of the radiation pattern of a single radiator in the antenna array," in *IEEE Antennas and Propagation Magazine*, vol. 57, no. 6, pp. 16-21, Dec. 2015, doi: 10.1109/MAP.2015.2481818.

[17] H. Matzner , M. Milgrom & S. Shtrikman, "Magnetoelectric symmetry and electromagnetic radiation", *Ferroelectrics*, 161:1, 213-219, 1994, doi: 10.1080/00150199408213369

[18] J. L. Young, "On the Exact Mutual Reactance of a Line Source Array: A Hilbert Transform Methodology," in *IEEE Transactions on Antennas and Propagation*, vol. 67, no. 3, pp. 1681-1687, March 2019, doi: 10.1109/TAP.2018.2888954.

[19] S. O. Rice, "Mathematical analysis of random noise," in *The Bell System Technical Journal*, vol. 23, no. 3, pp. 282-332, July 1944, doi: 10.1002/j.1538-7305.1944.tb00874.x.

[20] P. Bolli, F. Paonessa, G. Pupillo, G. Virone, M. Arts, A. Lingua, J. Monari, S. J. Wijnholds, "Antenna pattern characterization of the low-frequency receptor of LOFAR by means of an UAV-mounted artificial test source," in *Proc. SPIE, Ground-based and Airborne Telescopes* VI, 99063V (27 July 2016); https://doi.org/10.1117/12.2232419

[21] F. Paonessa et al., "First Results on the Experimental Validation of the SKA-low Prototypes Deployed in Australia Using an Airborne Test Source," in *XXXIIIrd General Assembly and Scientific Symposium of the International Union of Radio Science*, Rome, Italy, 2020, pp. 1-3, doi: 10.23919/URSIGASS49373.2020.9232190.

[22] Norman L. Johnson et.al., "Continuous Univariate Distributions", Volume 2, United Kingdom, Wiley, 1995.

[23] L. J. Greenstein, S. S. Ghassemzadeh, V. Erceg and D. G. Michelson, "Ricean K-Factors in Narrow-Band Fixed Wireless Channels: Theory, Experiments, and Statistical Models," in *IEEE Transactions on Vehicular Technology*, vol. 58, no. 8, pp. 4000-4012, Oct. 2009, doi: 10.1109/TVT.2009.2018549

[24] M. Kovaleva and K. F. Warnick, "Effect of Noise in Embedded Element Pattern Measurements on Mutual Impedance Matrix Extraction," in *17th European Conference on Antennas and Propagation (EuCAP)*, Florence, Italy, 2023, pp. 1-3, doi: 10.23919/EuCAP57121.2023.10133058.